EVALUATION OF BISTATIC FAR-FIELD QUANTITIES FROM NEAR-FIELD MEASUREMENTS

J. L. Leou and H. J. Li

Department of Electrical Engineering &
Graduate Institute of Communication Engineering
National Taiwan University
Taipei, Taiwan, Republic of China

1. INTRODUCTION

In bistatic radar applications it is often desirable to collect database about bistatic radar cross section (RCS), bistatic range profiles or bistatic microwave images of targets for target identification. These database can be established from field measurements. However, field measurements are expensive and it is difficult to control measurement parameters. Indoor measurements are usually preferable because parameters are more controllable and the results are repeatable. However the distance required to satisfy the far-field condition is much longer than the indoor dimension for many targets of interest.

Several near-field measurement techniques have been proposed to predict far-field antenna patterns [1–3]. In these techniques, the radiated field is measured by a small probe scanning over a large aperture.

If we replace the testing antenna by an object and illuminate the object by plane waves, then currents will be induced on the surface. The induced surface current plays the same role as the current source of the testing antenna. Therefore, we can use the same near-field measurement technique to measure the scattered near fields and from which to derive the far-field quantities. It is well known that the measured near-fields can be considered as the secondary sources [4] and the Fourier transform of the source distribution gives the far-field radiation pattern. For the near-field scattering problem it is also expected that the Fourier transform of the measured near-field will give the far-field scattering pattern. However, this is a bistatic scattering pattern for a given incident direction. To convert the bistatic scattering pattern into bistatic RCS a calibration procedure is required.

Far-field bistatic range profiles can be obtained by transmitting a narrow short pulse or a linear chirp signal or a burst of step-frequency signals if the transmitter and the receiver can be coherently connected. The derivation of far-field bistatic range profiles from near-field measurements is nontrivial. In this paper we will propose an algorithm to achieve that.

The generalized interpretation and prediction in far-field microwave imaging involving frequency and angular diversity have been discussed [5, 6]. An Ewald sphere representation for the Fourier space data in the monostatic and bistatic frequency diversity imaging has been established, and microwave images can be obtained by taking the inverse Fourier transform of the Fourier space data. In far-field microwave imaging, the Fourier space data are the measured far-field monostatic or bistatic range-corrected scattered field with range corrected with respect to a rotational center. In [7–9], several techniques have been proposed to extract the far-field quantities from near-field imaging. In this paper we will establish the relationship between the near-field measurements and the far-field quantities. We will show how to convert the near-field measurement data into the Ewald sphere representation. Furthermore, we will propose algorithms to reconstruct three-dimensional (3-D) images from near-field measurements. In the near-field measurement, it is more practical to obliquely illuminate the object. In that case, the Fourier space data should be properly converted. We will suggest how to convert the Fourier space data for oblique illumination.

In Section 2 we will discuss bistatic far-field RCS, range profiles and images. Relationship between near-field measurements and far-field quantities will be described in Section 3. The derivation of far-field bistatic RCS, bistatic range profiles and bistatic images from near-field measurements will be given in Section 3 too. Numerical and experimental results, especially for two-dimensional (2-D) case, will be discussed in Section 4. Conclusions are given in Section 5.

2. FORMULATION OF THE INTEGRAL EQUATIONS

Figure 1 shows a metallic object illuminated by a plane wave with wavenumber k. O is the reference point; $\hat{l}_i$ is the unit vector directed from the transmitting antenna to the reference point; $\hat{l}_r$ is the unit vector directed from the reference point to the receiving antenna; R_i and R_r are the distances from the reference point to the transmitter and receiver, respectively; β is the bistatic angle; $\hat{l}_p$ is the unit vector bisecting the transmitter and receiver; $\hat{n}(\bar{r}')$ is the unit vector normal to the surface at the point $\bar{r}'$. Under the far-field and physical optics (PO) approximation, the scattered field can be expressed as [5]

$$\bar{E}_s(\hat{l}_r, \hat{l}_i, k) = \frac{jkH_o}{2\pi\epsilon_o R_i R_r} e^{-jk(R_i+R_r)}$$
$$\int_{S_{ill}} \{(\hat{n} \times \hat{e}_i) - [(\hat{n} \times \hat{e}_i) \cdot \hat{l}_r]\hat{l}_r\} e^{jk(\hat{l}_r - \hat{l}_i)\cdot\bar{r}'} \, ds' \quad (1)$$

where H_o and $\hat{e}_i$ are the magnitude and unit vector of the incident magnetic field respectively and S_{ill} denotes the illuminated surface region of the object.

Let $\hat{e}_r$ represent the polarization of the receiving antenna. The quantity measured by the receiving antenna is given by

$$\Phi(\hat{l}_r, \hat{l}_i, k) = \bar{E}_s \cdot \hat{e}_r^* \quad (2)$$

where * represents the complex conjugate. Define the vector and scalar object scattering functions $\bar{O}(\bar{r}')$ and $O(\bar{r}')$ as

$$\bar{O}(\bar{r}') = (\hat{n} \times \hat{e}_i) - [\hat{l}_r \cdot (\hat{n} \times \hat{e}_i)]\hat{l}_r$$
$$O(\bar{r}') = \bar{O}(\bar{r}') \cdot \hat{e}_r^*. \quad (3)$$

Define the p-space vector $\bar{p}$ as

$$\bar{p} = k(\hat{l}_i - \hat{l}_r) = 2k \cos\frac{\beta}{2}\hat{l}_p. \quad (4)$$
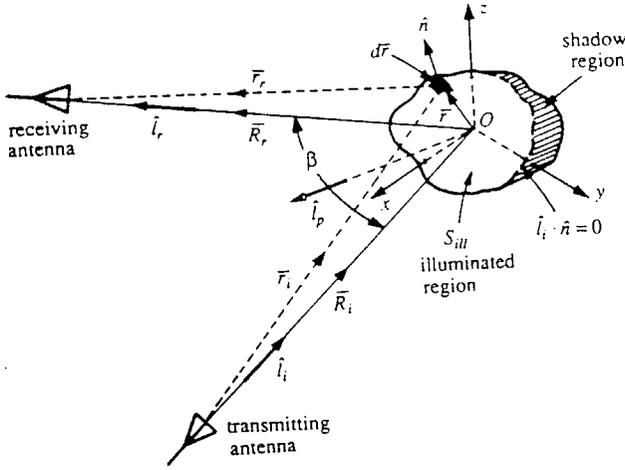
Figure 1. Scattering geometry of a metallic object.

The range-corrected scattered field can be expressed as

$$\Gamma(\hat{l}_r, \hat{l}_i, k) = \frac{2\pi\epsilon_o R_i R_r}{jkH_o} e^{jk(R_r + R_i)} \Phi(\hat{l}_r, \hat{l}_i, k). \qquad (5)$$

Substituting Eqs. (1–4) into Eq. (5), we have

$$\Gamma(\hat{l}_r, \hat{l}_i, k) = \Gamma(\bar{p}) = \int_{S_{ill}} O(\bar{r}') \, e^{j\bar{p}\cdot\bar{r}'} \, dS' \qquad (6)$$

where the quantity $\Gamma(\bar{p})$ is referred to as the p-space data or the Fourier space data. Note that $\Gamma(\bar{p})$ is a function of the incident direction, the receiving direction and frequency, but it is independent of the distances R_i and R_r.

There are three variables, $k, \hat{l}_r, \hat{l}_i$, which we can utilize to access the Fourier space data. Frequency diversity refers to the change of k; while angular diversity refers to the change of $\hat{l}_r$ or $\hat{l}_r - \hat{l}_i$. The Ewald sphere construction process has been introduced to describe the accessed data graphically [5]. For a given incident vector, $\bar{k}_i = k\hat{l}_i$, the corresponding Ewald sphere is a sphere centered at $\bar{k}_i$ and with radius k as shown in Fig. 2, where the quantities $\bar{k}_r = k\hat{l}_r$ and $\bar{p} = k(\hat{l}_r - \hat{l}_i)$.

Let (θ_i, ϕ_i) be the incident direction and (θ, ϕ) be the observation direction. Then $k\hat{l}_i$, $k\hat{l}_r$ and $\bar{p}$ can be expressed as
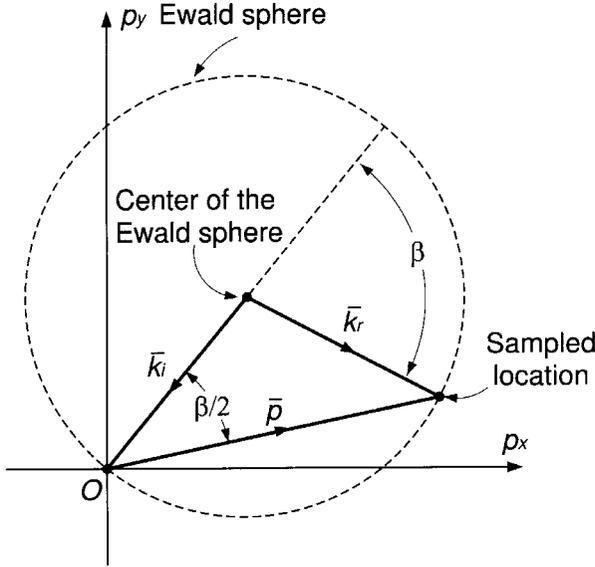
Figure 2. Ewald sphere construction process.

$$k\hat{l}_i = k(\sin\theta_i\cos\phi_i\hat{x} + \sin\theta_i\sin\phi_i\hat{y} + \cos\theta_i\hat{z}) = k_{ix}\hat{x} + k_{iy}\hat{y} + k_{iz}\hat{z} \quad (7)$$

$$k\hat{l}_r = k(\sin\theta\cos\phi\hat{x} + \sin\theta\sin\phi\hat{y} + \cos\theta\hat{z}) = k_x\hat{x} + k_y\hat{y} + k_z\hat{z} \quad\quad (8)$$

$$\bar{p} = (k_x - k_{ix})\hat{x} + (k_y - k_{iy})\hat{y} + (k_z - k_{iz}\hat{z}) = p_x\hat{x} + p_y\hat{y} + p_z\hat{z}. \quad (9)$$

The equation that describes the Ewald sphere for a given $\bar{k}_i$ is given by

$$k^2 = k_x^2 + k_y^2 + k_z^2$$
$$= (p_x + k_{ix})^2 + (p_y + k_{iy})^2 + (p_z + k_{iz})^2. \quad\quad (10)$$

Given any value of $(\hat{l}_r, \hat{l}_i, k)$, we have a Fourier space data point. A collection of Fourier space data points can be obtained by varying k, $\hat{l}_r$, $\hat{l}_i$ or $\hat{l}_r - \hat{l}_i$. For the bistatic frequency and angular diversity case, $\bar{p} = k(\hat{l}_r - \hat{l}_i)$, changing the direction of the receiving antenna will change the direction of $\bar{p}$ and changing the frequency will change the radius of the sphere. The Fourier space data for different frequency and bistatic angle are distributed on spheres (or circles when $\theta = 90°$) as shown in Fig. 2. For a given bistatic angle β, the sampled Fourier space data are distributed on the radial line along the direction of $\hat{l}_p$.

Bistatic radar cross section information is important in missile applications; range profiles are important feature vectors for target identification; and microwave images have applications in diagnosing hot spots of a target. These three quantities can be obtained from the Fourier space data. The relation between the Fourier space data and the bistatic RCS can be derived from the definition of the bistatic RCS. By definition, the bistatic RCS for a given polarization pair $(\hat{e}_i, \hat{e}_r)$ is given by

$$\sigma_b = (4\pi R_i R_r)^2 \frac{|\bar{E}_s \cdot \hat{e}_r|^2}{|\bar{E}_o|^2}. \tag{11}$$

Using Eq. (2), Eq. (5) and the fact that $|\bar{E}_i| = \eta|\bar{H}_i|$ we can rewrite Eq. (7) as

$$\sigma_b = (4\pi R_i R_r)^2 \frac{|\Phi(\hat{l}_r, \hat{l}_i, k)|^2}{|\eta\bar{H}_i|^2} = \frac{k^2 |\Gamma(\bar{p})|^2}{\pi}. \tag{12}$$

where E_i, H_i and η are incident electric field, incident magnetic field and free space intrinsic impedance, respectively.

In a high resolution radar, the target's bistatic range profile can be obtained by transmitting a very short pulse or by taking the inverse Fourier transform of the sampled Fourier space data distributing along a radial line. The three-dimensional microwave bistatic image can be obtained by taking the inverse Fourier transform of the 3-D Fourier space data directly. Note that the Fourier space data are the range-corrected scattered fields rather than the measured fields. Therefore, an accurate calibration procedure is required in order to obtain range profiles and microwave images.

3. NUMERICAL SOLUTION OF INTEGRAL EQUATION

The relation between near-field measurements and far-field pattern can be established by using the plane wave expansions [1–3]. Consider Fig. 3, where a plane wave impinges on a metallic object and its scattered fields are measured in the near-field region along $x = -d$. The near-field scattered field $\bar{E}(\bar{r})$ can be expressed as [9]

$$\bar{E}(\bar{r}) = \frac{1}{4\pi^2} \left\{ \iint \frac{-\omega\mu_o}{2\gamma} e^{-j\gamma d} \left[\iint_{S_{ill}} [\bar{J}_s(\bar{r}') - \hat{k}(\hat{k} \cdot \bar{J}_s(\bar{r}'))] e^{j\bar{k}\cdot\bar{r}'} ds' \right] \right.$$
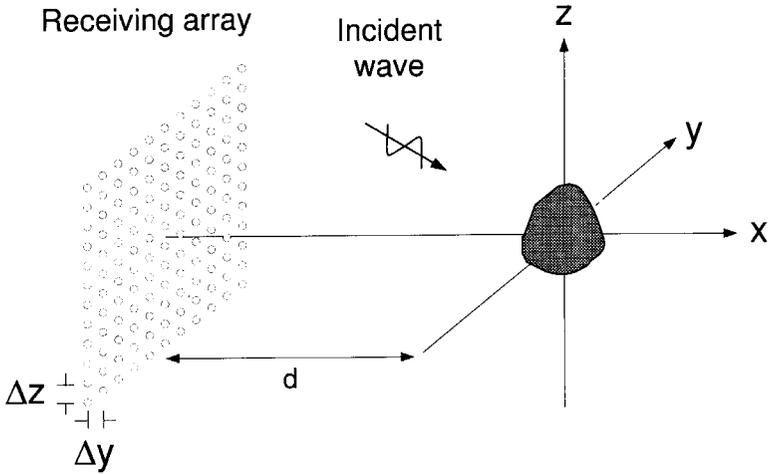$$\left. e^{-j(k_y y + k_z z)} dk_y dk_z \right\} \tag{13}$$

Figure 3. The near-field receiving configuration.

where γ, k_y, k_z are the angular spectrum components of the plane wave, and γ and $\bar{k}$ are respectively given by

$$\gamma = \begin{cases} \sqrt{k^2 - k_y^2 - k_z^2} & k^2 \geq (k_y^2 + k_z^2) \\ -j\sqrt{k_y^2 + k_z^2 - k^2} & k^2 < (k_y^2 + k_z^2) \end{cases} \tag{14}$$

$$\bar{k} = k_x \hat{x} + k_y \hat{y} + k_z \hat{z} = \pm\gamma\hat{x} + k_y\hat{y} + k_z\hat{z}. \tag{15}$$

The quantity $\bar{J}_s(\bar{r}')$ in Eq. (13) is the induced surface current density. Under the PO approximation $\bar{J}_s(\bar{r}')$ is given by

$$\bar{J}_s(\bar{r}') = \begin{cases} 2\hat{n}(\bar{r}') \times \bar{H}_i(\bar{r}') & \text{illuminated region} \\ 0 & \text{elsewhere} \end{cases} \tag{16}$$

where $\bar{H}_i$ is the incident magnetic field and is given by

$$\bar{H}_i(\bar{r}') = H_o e^{-jk\hat{l}_i \cdot \bar{r}'} \hat{e}_i. \tag{17}$$

The quantity $\bar{k}$ in Eq. (15) is the propagation vector of the observation direction. Letting $\bar{k} = k\hat{l}_r$ and using Eqs. (16) and (17), we have

$$[\bar{J}_s(\bar{r}') - \hat{l}_r(\hat{l}_r \cdot \bar{J}_s(\bar{r}'))]e^{j\bar{k}\cdot\bar{r}'}$$
$$= 2H_o\{\hat{n}(\bar{r}') \times \hat{e}_i - [(\hat{n}(\hat{r}') \times \hat{e}_i) \cdot \hat{l}_r]\hat{l}_r\}e^{jk(\hat{l}_r - \hat{l}_i) \cdot \bar{r}'}. \tag{18}$$

Comparing Eq. (18) and Eq. (1), we observe that both equations contain the term $\{\hat{n}(\bar{r}') \times \hat{e}_i - [(\hat{n}(\hat{r}') \times \hat{e}_i) \cdot \hat{l}_r]\hat{l}_r\}$.

Using Eq. (3) and Eq. (6), the near-field scattered field in Eq. (13) can be expressed as

$$\bar{E}^s(x = -d, y, z) = \frac{1}{4\pi^2} \iint \frac{-\omega\mu_o H_o}{\gamma} e^{-j\gamma d} \bar{\Gamma}(\bar{p}) e^{-j(k_y y + k_z z)} dk_y dk_z.$$
(19)

From Eq. (19), one can find that $\bar{E}^s(x = -d, y, z)$ and $\frac{-\omega\mu_o H_o}{\gamma} e^{-j\gamma d} \bar{\Gamma}(\bar{p})$ are a 2-D Fourier transform pair. Therefore, we can obtain $\bar{\Gamma}(\bar{p})$ by

$$\bar{\Gamma}(\bar{p}) = \frac{-\gamma}{kE_o} e^{j\gamma d} \iint \bar{E}^s(x = -d, y, z) e^{j(k_y y + k_z z)} dy dz$$
(20)

Eq. (20) implies that the far-field Fourier space data can be derived by taking the 2-D Fourier transform of the near-field measurement data.

As mentioned in the previous section, the Fourier space data $\bar{\Gamma}(\bar{p})$ represents the far-field range-corrected bistatic scattered field. Therefore, the bistatic field at any observation direction can be obtained by using of Eq. (8) and substituting a suitable (k_y, k_z) into Eq. (20). The bistatic RCS can then be derived from Eq. (12).

The Fourier space data $\bar{\Gamma}(\bar{p})$ can also be obtained by applying the fast Fourier transform (FFT) to Eq. (19). With this method, the sampled data points will be at $p_y = m\Delta k_y - k_{iy}$, $p_z = n\Delta k_z - k_{iz}$ and $p_x = \sqrt{k^2 - (m\Delta k_y)^2 - (n\Delta k_z)^2} - k_{ix}$, where (m, n) are integers. With the normal incidence (i.e., $\theta_i = 90°$, $\phi_i = 0°$), or $k_{iy} = k_{iz} = 0$, the sampled Fourier space data points for various frequencies on the $\theta = 90°$ plane are shown in Fig. 4(a). For the oblique incidence (i.e., $\theta_i = 90°$, $\phi \neq 0°$ or $k_{iz} = 0$, $k_{iy} \neq 0$), the sampled data points are shown in Fig. 4(b). It is important to have the correct locations of the sampled Fourier space data. Otherwise, the reconstructed quantities such as microwave images will not be correct.

To obtain the far field quantities, it is more convenient to express $\bar{\Gamma}(\bar{p})$ in a spherical coordinate. Given a observation direction (θ, ϕ), $\bar{\Gamma}(\bar{p})$ can be expressed as

$$\bar{\Gamma}(\bar{p}) = \Gamma_\theta \hat{\theta} + \Gamma_\phi \hat{\phi}$$
(21)

where Γ_θ and Γ_ϕ are given by

$$\Gamma_\theta = \bar{\Gamma} \cdot \hat{\theta} = \Gamma_x \cos\theta \cos\phi + \Gamma_y \cos\theta \sin\phi - \Gamma_z \sin\phi$$
(22)

$$\Gamma_\phi = \bar{\Gamma} \cdot \hat{\phi} = -\Gamma_x \sin\phi + \Gamma_y \cos\phi.$$
(23)

Using Eq. (20), the quantities Γ_x, Γ_y and Γ_z can be obtained by collecting x-, y- and z-polarized near field of $\bar{E}^s(x = -d, y, z)$, respectively. With the expression of Γ_θ and Γ_ϕ, we can obtain bistatic quantities for various polarization combination. For example, with a z-polarized incident wave, we measure $E_{y1}(x = -d, y, z)$ and $E_{z1}(x = -d, y, z)$. With a y-polarized wave, we measure $E_{y2}(x = -d, y, z)$ and $E_{z2}(x = -d, y, z)$. For an arbitrarily polarized incident wave $\hat{e}_i = \dfrac{a\hat{y} + b\hat{z}}{\sqrt{|a|^2 + |b|^2}}$, the bistatic far field will be the linear combination of $\bar{\Gamma}_1(\bar{p})$ and $\bar{\Gamma}_2(\bar{p})$. We can obtain polarization diversity by varying the incident wave $\hat{e}_i$ and the unit polarization vector of the receiving antenna $\hat{e}_r$, accordingly.

Summarizing the results, we describe the procedures to obtain the following desirable far-field quantities:

I. The bistatic far-field at wavenumber k:
1. Illuminate the object by a plane wave with wavenumber k.
2. Use a probe oriented in both the $\hat{y}$ and $\hat{z}$ directions to measure the near-field transverse components E_y and E_z along a planar surface.
3. Use Eqs. (20), (22) and (23) to calculate the bistatic far-field.

II. The bistatic range profile at a given direction (θ, ϕ):
1. The desired coordinates of Fourier space data points are along a radial line and they are given by

$$p_x = k(\sin\theta\cos\phi - \sin\theta_i\cos\phi_i) \tag{24}$$
$$p_y = k(\sin\theta\sin\phi - \sin\theta_i\sin\phi_i) \tag{25}$$
$$p_z = k(\cos\theta - \cos\theta_i). \tag{26}$$

2. Find the Fourier-space data at (p_x, p_y, p_z) from the nearest available sampled data points using an interpolation process.
3. Take the Fourier transform of the interpolated data with respect to p and the result is the bistatic range profile at the given (θ, ϕ) direction.

III. The microwave image for a given observation angular window $(\theta_{min}, \theta_{max})$ and (ϕ_{min}, ϕ_{max}):
1. Set the Fourier-space data outside the observation angular window equal to zero.
2. In order to use the efficient FFT algorithm, the new sampled points should be in a rectangular grid format.
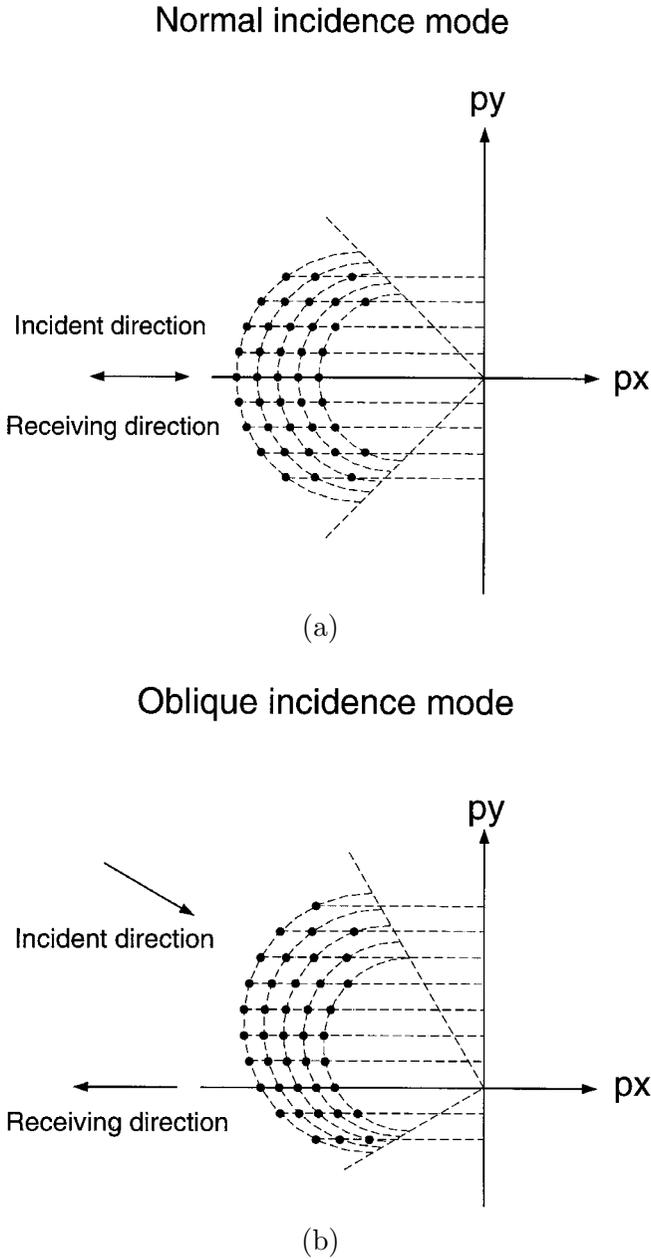
Normal incidence mode

(a)

Oblique incidence mode

(b)

Figure 4. Accessed Fourier space by frequency and angular diversity with (a) normal incidence mode, (b) oblique incidence mode.

3. Obtain the Fourier-space data of the above rectangular grid points from the nearest available sampled points using an interpolation process.
4. Apply the 3-D Fourier transform to the interpolated Fourier-space data to reconstruct the image. The resultant image is the 3-D bistatic image of the object for the given observation angular window.

4. RESULTS AND OBSERVATIONS

In this section computer simulation and experiment setup for bistatic range profiles and 3-D image reconstruction are studied. Results obtained from the far-field data and the near-field data are compared. Finally, a 2-D near-field imaging experiment is provided.

4.1 Simulation Results

Assume that the testing object consists of thin wire scatterers. The geometry of the object is shown in Fig. 5. Four vertical wires, each with a length of $20\,\mathrm{cm}$, are centered at $(-25\,\mathrm{cm},\ 0\,\mathrm{cm},\ 0\,\mathrm{cm})$, $(0\,\mathrm{cm},\ 0\,\mathrm{cm},\ 0\,\mathrm{cm})$, $(-15\,\mathrm{cm},\ 20\,\mathrm{cm},\ 5\,\mathrm{cm})$ and $(-15\,\mathrm{cm},\ -20\,\mathrm{cm},\ 5\,\mathrm{cm})$, respectively. A z-polarized plane wave is incident in the $+x$ direction, i.e., we have $\theta_i = 90°$, $\phi_i = 0°$. The frequency is uniformly incremented from $7\,\mathrm{GHz}$ to $13\,\mathrm{GHz}$ with a total of 64 frequency points. The method of moment is employed to calculate the scattered field, where the mutual coupling among wires is negligible due to their adequate separations.

In the near-field receiving configuration, the receiving plane is on the $x = -4\,\mathrm{cm}$ surface. A y-polarized probe and a z-polarized probe are used to collect the near-field data. To avoid aliasing effect, the sampling spacing Δd and the frequency increment Δf should satisfy

$$\Delta d \leq \frac{\lambda_{min}}{2} \tag{27}$$

and

$$\Delta f \leq \frac{c}{2D_{max}} \tag{28}$$

respectively, where λ_{min} and D_{max} are the minimum wavelength and the maximum dimension of the testing object respectively. In the following, Δd is chosen as $1\,\mathrm{cm}$ and the synthesized aperture size
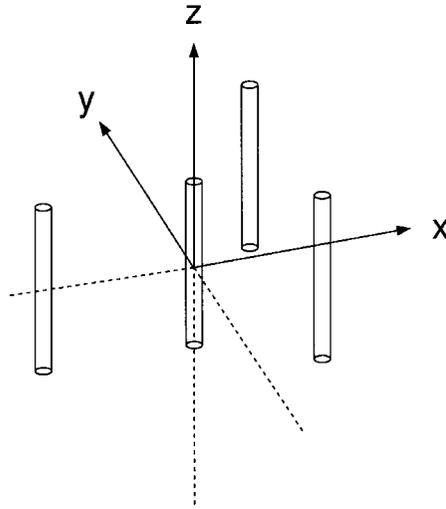
Wires are centered at
(-25, 0, 0) (0, 0, 0) (-15, 20, 5) (-15, -20, 5)

Figure 5. Geometry of thin wire scatterers.

is $128\,\mathrm{cm} \times 128\,\mathrm{cm}$. The frequency increment is $\Delta f = 100\,\mathrm{MHz}$ and the number of frequency points is 64.

We first calculate the y-polarized and z-polarized received field $\bar{E}^s(x = -d, y, z)$ at each sampled position and each sampled frequency and then use Eq. (20) to obtain the Fourier space data $\Gamma(\bar{p})$.

As we have mentioned in Section 3, bistatic range profiles can be derived from the received near field data. Given an observation direction (θ_r, ϕ_r), we use Eqs. (24), (25), and (26) to calculate the corresponding rectangular p-space coordinate. Then an interpolation algorithm can be applied to find the received Fourier space data. The bistatic range profile at the given direction can be obtained by taking the inverse Fourier transform of the interpolated Fourier space data. The dashed curve of Fig. 6 is the range profile at $\theta_r = 90°$, $\phi_r = 180°$, which is in the opposite direction of the incident wave and has a zero bistatic angle. The bistatic range profile can also be derived from the far field data directly calculated using the moment method. The result is shown in the solid curve of Fig. 6. One can see that these two curves match very well. We also compare bistatic range profiles at $\theta_r = 90°$, $\phi_r = 165°$ (which is on the x-y plane) and at $\theta_r = 75°$, $\phi_r = 180°$
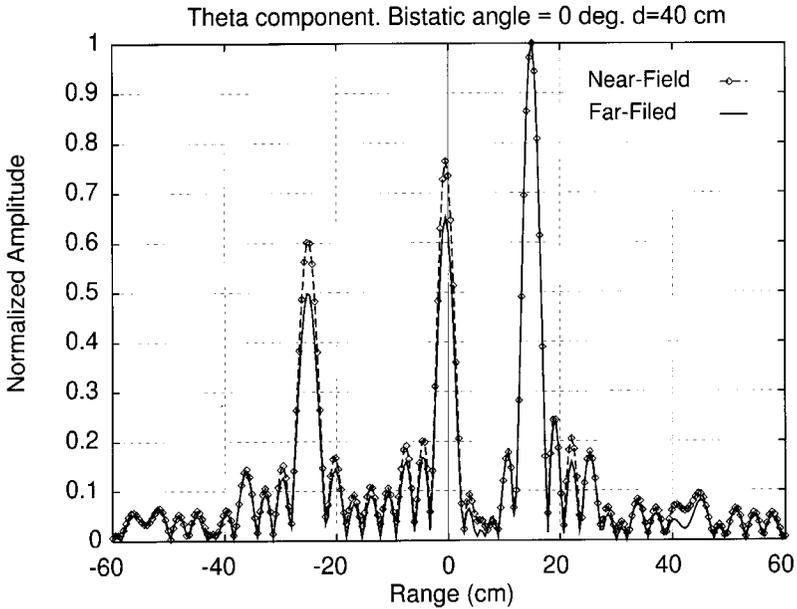
Figure 6. Near-field and far-field bistatic range profiles with a bistatic angle of $0°$.

(which is on the x-z plane) obtained from the near-field data and the far-field data, and the results are shown in Fig. 7 and Fig. 8. Both directions have a bistatic angle of $15°$. However, the former is in the specular direction and the latter is not. The two curves in Fig. 8 do not match very well and the dashed curve has a poorer resolution. Note that the Fourier space data obtained from near-field measurements is not a direct method. In the above receiving configuration, the scanning aperture does not contain fields scattered from all directions. For example, the field scattered in directions outside the following coverage

$$\tan^{-1} \frac{40}{64} = 32° < \theta < 148° = 180° - 32° \tag{29}$$

$$90° + 32° = 122° < \phi < 270° - 32° = 238° \tag{30}$$

will not be received by the scanning probe. This will limit the accuracy of the derived Fourier space data and therefore the bistatic range profile.

For near-field images, the eight-nearest-neighbor interpolation algorithm is employed to obtain the Fourier space data in the rectangular
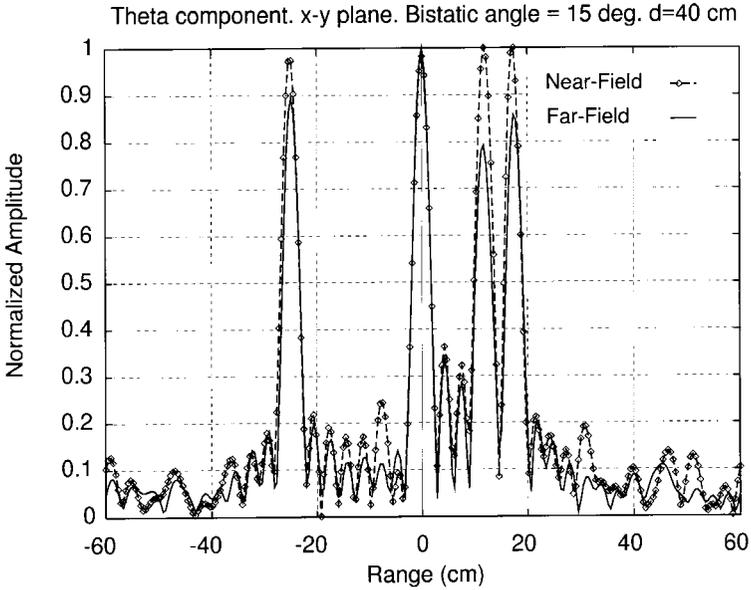
Theta component. x-y plane. Bistatic angle = 15 deg. d=40 cm

Figure 7. Near-field and far-field bistatic range profiles with a bistatic angle of $15°$ when $\theta_r = 90°$, $\phi_r = 165°$.

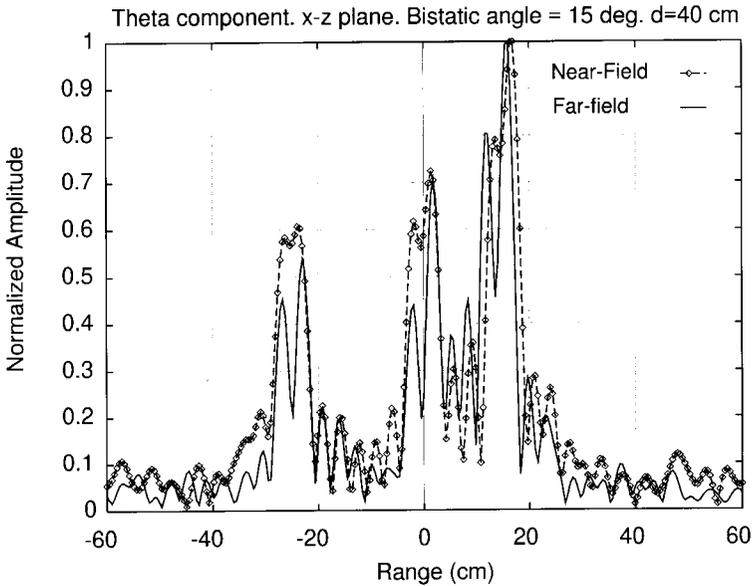Theta component. x-z plane. Bistatic angle = 15 deg. d=40 cm

Figure 8. Near-field and far-field bistatic range profiles with a bistatic angle of $15°$ when $\theta_r = 75°$, $\phi_r = 180°$.

grid format, so that the 3-D FFT can be directly applied to the Fourier space data to obtain 3-D images.

It has been indicated that the appearance of reconstructed image depends on the observation angular window available [5, 10]. With the near-field receiving configuration, the maximum angular coverage of the Fourier space is spanned within $0° < \theta < 180°$ and $90° < \phi < 270°$. To predict the reconstructed image for a given angular window, we can artificially set the Fourier space data outside the given window to zero and then apply the 3-D FFT to the windowed Fourier space data. Therefore, the reconstructed image for any given angular window can be obtained. Figures 9(a) and 10(a) show the Fourier space data for the angular window $0° < \theta < 60°$, $120° < \theta < 180°$, $90° < \phi < 270°$ and for the window $60° < \theta < 120°$, $90° < \phi < 270°$ respectively. The corresponding reconstructed images are shown in Figs. 9(b) and 10(b) respectively. In Fig. 9, the angular window does not contain the specular aspects, which are in the plane of $\theta = 90°$. In this case the dominant contributions to the scattered field are from the end points of wires. We can easily see that the reconstructed image of Fig. 9(b) reflects end points of the wires. This is consistent with the prediction made by [5, 10]. While in Fig. 10, the angular window contains the specular aspects. Therefore the shape of wires is clearly reconstructed. From the above examples we can make following conclusions: With the near-field configuration, we can derive bistatic far field from the received near field. We can obtain the 3-D image of any observation window by first applying a suitable angular window to the derived Fourier space data and then taking the 3-D FFT of the windowed data.

4.2 Experimental Results

Figure 11 shows the setup of our near-field experiment system. An Arra X820 rectangular horn antenna is used to illuminate the testing object. A probe, an open-ended WR-90 rectangular waveguide, is mounted on a NSI-233 planar scanner to receive the scattered near field. The planar scanner is controlled by stepping motors and can move along the y-direction and z-direction. The measurement system also includes an Hughes 8010H traveling wave tube amplifier, an Avantek AWT-18235 low noise amplifier, and a HP8510C network analyzer. All measurements are controlled by a personal computer via an IEEE-488 bus.
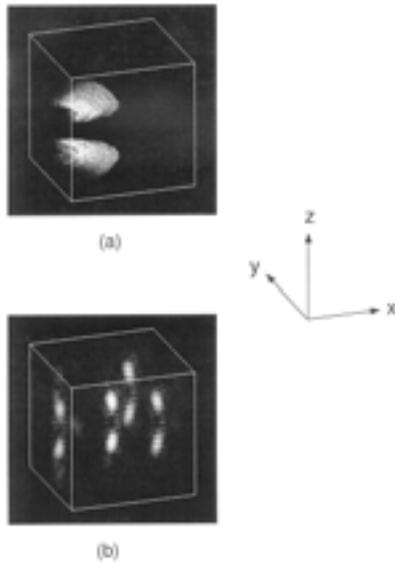
Figure 9. Near-field bistatic image for angular window $\phi = 90° \sim$ 270° and $\theta = 0° \sim 60°$, 120° $\sim$ 180°. (a) Fourier space data, (b) reconstructed image.
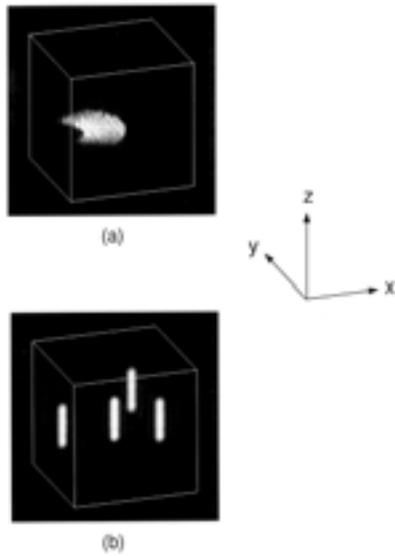

Figure 10. Near-field bistatic image for angular window $\phi = 90° \sim$ 270° and $\theta = 60° \sim 120°$. (a) Fourier space data, (b) reconstructed image.

Note that in the above configuration, the object is obliquely illuminated rather than normally illuminated and the angular range covered by the scanner is $\phi_c = 2\tan^{-1}\frac{D}{2d}$, where D is the total scanning length and d is the distance between the reference point and the scanning plane. In earlier simulation, we can calculate the theoretical range-corrected field for each frequency. In the measurement, however, we have to find a calibration method so that range-corrected fields can be accurately obtained.

The proposed calibration procedure is given as follows:
1. Use the horn antenna to illuminate the testing object.
2. Use the y-polarized and z-polarized probe to measure the scattered field at each scanning position and denote them by $E_{t,y}^m(-d, y, z, k)$ and $E_{t,z}^m(-d, y, z, k)$.
3. Replace the testing object by a reference object, repeat step 2 and denote them by $E_{r,y}^m(-d, y, z, k)$ and $E_{r,z}^m(-d, y, z, k)$. It is preferable that the reference object is a point-like object, e.g., a small sphere if the scattering aperture is along the y-z plane.
4. Remove the reference object, repeat step 2, and the measured fields are the clutter fields. Denote them as $E_{c,y}^m(-d, y, z, k)$ and $E_{c,z}^m(-d, y, z, k)$.
5. The calibrated field can be obtained by subtracting the clutter field obtained in step 4 from those obtained in 2 and 3 respectively. Denote them by $E_{t,i}$ and $E_{r,i}$. These calibrated field are give by

$$E_{t,i}(-d, y, z, k) = E_{t,i}^m(-d, y, z, k) - E_{c,i}^m(-d, y, z, k) \quad i = y, z \quad (31)$$
$$E_{r,i}(-d, y, z, k) = E_{r,i}^m(-d, y, z, k) - E_{c,i}^m(-d, y, z, k). \quad (32)$$

From the calibrated data, we can obtain the range-corrected Fourier space data as follows:
1. Take the 2-D Fourier transform of $E_{t,i}(-d, y, z, k)$ with respect to y and z for each frequency k, and denote it by $\tilde{E}_{t,i}(k_y, k_z, k)$.
2. Take the 2-D Fourier transform of $E_{r,i}(-d, y, z, k)$ with respect to y and z for each frequency k and denote it by $\tilde{E}_{r,i}(k_y, k_z, k)$.
3. The range-corrected Fourier space data of the testing object can be obtained by

$$\Gamma_i(k_y, k_z, k) = \frac{\tilde{E}_{t,i}(k_y, k_z, k)}{\tilde{E}_{r,i}(k_y, k_z, k)} \, |\rho_o(k_y, k_z, k)|^{1/2} \quad i = y, z \quad (33)$$
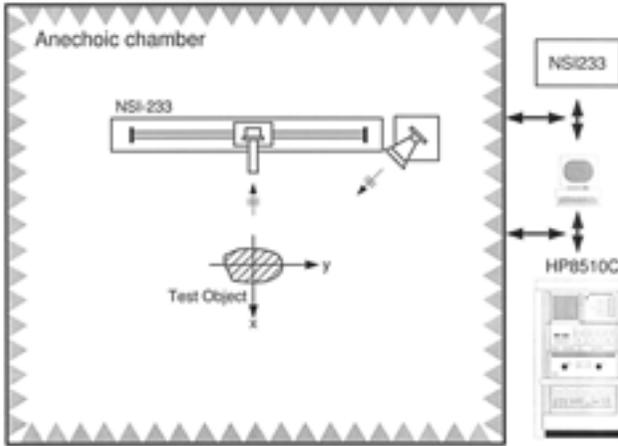
Figure 11. Experiment setup for the near-field measurement.

where $\rho_o(k_y, k_z, k)$ is the theoretical far field bistatic RCS of the reference object, which can be numerically calculated for a given shape of the reference object and a given illumination.

The division of $\tilde{E}_{r,i}(k_x, k_y, k)$ in Eq. (33) can result in a large error if $\tilde{E}_{r,i}(k_y, k_z, k)$ is small. To see this, note that k_y, k_z represent the angular spectrum, or the propagation direction of the scattered field. Relations between the observation direction (θ, ϕ) and (k_x, k_y, k_z) are given in Eq. (8). Note that after applying the 2-D FFT, the angular support of the Fourier space is the half-space, $0° < \theta < 180°$ and $90° < \phi < 270°$. However, in the near-field measurement arrangement shown in Fig. 12 , the extension of ϕ_c is $2\tan^{-1}(\frac{d}{2D})$. The field scattered by the testing object or the reference object will not be received by the probe when the scattering direction is beyond ϕ_c. Therefore, $\tilde{E}_{t,i}(k_y, k_z, k)$ and $\tilde{E}_{r,i}(k_x, k_y, k)$ will be very small when the angular spectrum (k_x, k_y) is beyond the extension angle. In those regions, the division of $\tilde{E}_{r,i}(k_x, k_y, k)$, can result in large a error. Therefore, $\Gamma_i(k_x, k_y, k)$ outside the extension coverage angle ϕ_c should be discarded.

In the following experiment, the testing object consists of three vertical thin cylinders with lengths of $30\,\mathrm{cm}$ and centers located at $(-4\,\mathrm{cm},\ 6\,\mathrm{cm})$, $(12\,\mathrm{cm},\ 0\,\mathrm{cm})$ and $(0\,\mathrm{cm},\ -8\,\mathrm{cm})$. The illuminating wave is z-polarized and the incident angle is $\phi_i = 131°$.
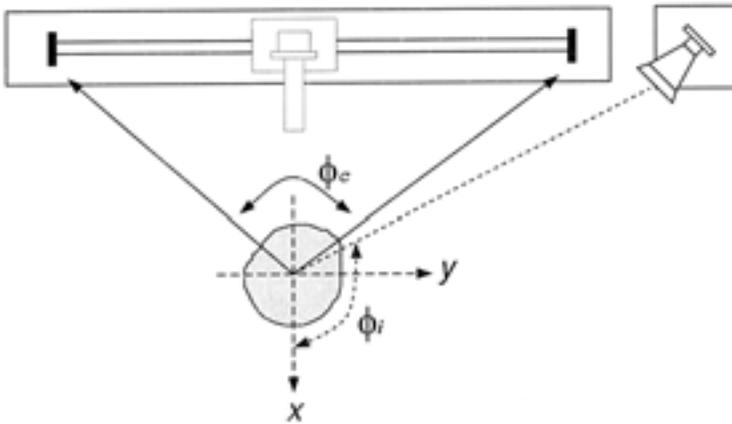
Figure 12. Effective angular coverage of the scanning aperture.

Although the scanning aperture can be moved in both the y and z directions, the scanner is designed to record the data at a single frequency for each scanning process. If we use N step frequencies, we have to repeat N times of 2-D scanning. The measurement would take a long time and the scanner often failed during experiment. Therefore we only scan the probe in the y direction and the following experiment is a 2-D near-field imaging. Because the probe is only scanned along one direction, we can use a small vertical cylinder instead of a small sphere as the reference object. In this experiment, a small vertical cylinder with radius $0.5\,\mathrm{cm}$ and length $30\,\mathrm{cm}$ is used as the reference object. Its center is chosen as the coordinate origin.

The receiving probe is scanned along the y-direction with 1 cm increment and has a total scanning length of 86 cm. The scanning line is at a distance $d = 60\,\mathrm{cm}$ from the reference point. The frequency is uniform sampled from $8\,\mathrm{GHz}$ to $12\,\mathrm{GHz}$ with a total of 51 frequency points.

We measure the clutter field, the scattered field of the reference object and the testing object at each scanning position and each frequency. We then follow the procedure as stated above to obtain the range-corrected Fourier space data (Fig. 13(a)). We retain only those data within the extension angle ϕ_c and discard all other data outside ϕ_c. Note that the factor of oblique incidence has been considered in the Fourier space data as mentioned in Fig. 4(b). We then take the inverse Fourier transform of the Fourier space data and the result is
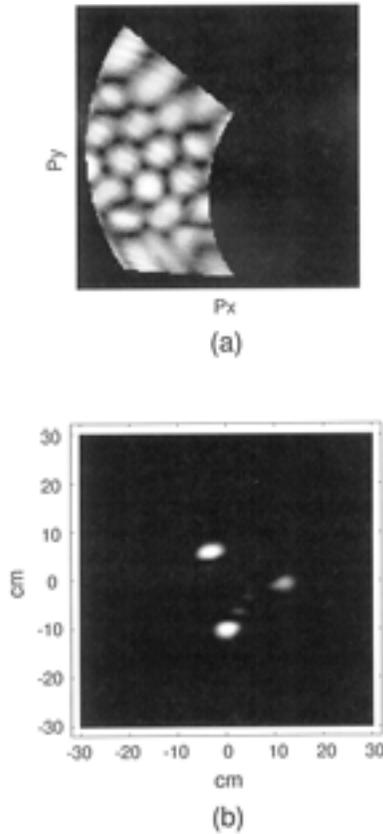
Figure 13. (a) The range-corrected Fourier space data and (b) the reconstructed image.

shown in Fig. 13(b). A clear three-point image is obtained. It was shown that, with an inverse synthetic aperture radar imaging technique of frequency diversity and bistatic angular diversity moving on the $\theta = 90°$ plane, the reconstructed image would be the projection of the object [5, 10]. We can see that Fig. 13(b) is the projection image of the testing object. This example verifies the effectiveness of our proposed calibration procedure and near-field image reconstruction algorithm.

5. CONCLUSIONS

We have studied the relationship between the Ewald sphere representation and the bistatic Fourier space data and described the procedure to obtain far field quantities, including bistatic RCS, bistatic range profiles and bistatic images, from the Fourier space data. We then described the relationship between the Fourier space data and the near-field measurements, and discussed how to obtain the Fourier space data in the Ewald sphere when the object is normally or obliquely illuminated and its scattered fields are received by a probe scanning over a planar aperture. We also showed how to obtain far field quantities from near field measurements. We have carried out the simulation of near-field configuration. The moment method is used to calculate the near fields and from those data, we can derive bistatic range profiles and 3-D images. We also setup a near field measurement system and propose a calibration procedure so that the range-corrected Fourier space data can be accurately obtained. A focused projective image has been obtained from near field measurements with 1-D scanning. Simulation and experimental results have verified the effectiveness of our algorithms.

Note that in our derivation we have assumed that the antenna pattern of the receiving probe is omnidirectional. We have also assumed that the object is illuminated by a plane wave. In fact, the probe has its own radiation pattern and the wave illuminated by a horn is not a plane wave but a spherical wave. Techniques for probes pattern compensation have been proposed for antenna near field measurements [1]. These techniques can also be applied to this problem. However, when the object is illuminated by a spherical wave, the relationship between the Fourier space data and near-field measurements is more complicated and it needs some further investigation [11].

REFERENCES

1. Joy, E. B., "Basic theory of probe-compensated near-field measurements," *IEEE Trans. on Antennas Propagation,* AP-26, No. 3, 373–379, May 1978.
2. Wolf, E., "Three-dimensional structure determination of semi-transparent objects from holographic data," *Optics Communications,* Vol. 1, No. 4, 153–156, September/October 1969.

3. Appel-Hansen, J., "Antenna Measurements", *The Handbook of Antenna Design* , Vol. 1, Ch. 8, Peter Peregrius Ltd., London, 1982.

4. Harrington, R. F., *Time Harmonic Electromagnectic Field* , N. Y., McGraw-Hill, 1961.

5. Li, H. J., F. L. Lin, Y. Shen, and N. H. Farhat, "A generalized interpretation and prediction in microwave imaging involving frequency and angular diversity," *J. Electromagnetic Waves and Applic.,* Vol. 4, No. 5, 415–430, 1990.

6. Farhat, N. H., C. L. Werner, and T. H. Chu, "Prospect for three-dimensional projective and tomographic imaging radar network," *Radio Science,* Vol. 19, No. 5, 1347–1355, 1984.

7. Li, H. J., and F. L. Lin, "Near Field Imaging for conducting Objects," *IEEE Trans. on Antenna and Propagation*, Vol. AP-39, 600–605, May 1991.

8. Huang, G. T. and H. J. Li, "Evaluation of far-field RCS from near-field measurements using a near-field imaging technique," *Proc. Natl. Sci. Counc. ROC(A)*, Vol. AP-17, No. 5, 353–358, 1993.

9. Chu, T. H. and D. B. Lin, "Microwave diversity imaging of perfectly conducting objects in the near-field region." *IEEE Trans. on Microwave Theory and Techniques*, Vol. 39, No. 3, March 1991.

10. Li, H. J., N. H. Farhat, Y. Shen, and C. L. Werner, "Image understanding and interpretation in microwave diversity imaging," *IEEE Trans. on Antennas and Propagation,* Vol. 37, No. 8, 1048–1057, 1989.

11 LaHaie, I. J. "Radar imaging and RCS measurement in the near field," *1993 IEEE AP-S Workshop,* 2, July, 1993.